ChemComm

COMMUNICATION

View Article Online
View Journal | View Issue

Cite this: *Chem. Commun.*, 2019, **55**, 11059

Received 16th July 2019,
Accepted 19th August 2019

DOI: 10.1039/c9cc05490a

rsc.li/chemcomm

A polar-hydrophobic ionic liquid induces grain growth and stabilization in halide perovskites†

Dan Liu,‡[ab] Zhipeng Shao,‡[c] Jianzhou Gui,[a] Min Chen,[b] Mingzhen Liu,[d] Guanglei Cui,[c] Shuping Pang[c] and Yuanyuan Zhou*[b]

The addition of a polar-hydrophobic methylammonium trifluoroacetate ionic liquid tailors the hydrophobicity of halide-perovskite precursor solutions and assists in grain growth. This unique additive also functionalizes the grain boundaries *via* polar–polar interactions, thereby enhancing the optoelectronic properties and chemical stability of perovskites. This study opens the door to the solution hydrophobicity control towards high-performance perovskite devices.

Hybrid perovskite (HP) materials have recently attracted a huge amount of attention in the field of solar cells, primarily because of their outstanding optoelectronic properties and facile solution-processability.[1–3] Since the invention of perovskite-based solar cells (PSCs) by Miyasaka *et al.*,[3] the power conversion efficiency (PCE) of PSCs has climbed rapidly, and now surpassed 24%.[4] Such a swift development of PSCs has been attributed to the advances in understanding of the solution chemistry of perovskites, which has led to numerous innovations in processing HP thin films with desirable morphologies and microstructures. In particular, the effects of precursor-solution parameters such as viscosity, compositions, solvent volatility, pH, and solute gelation degree on perovskite crystallization have been well studied.[5–8] However, in the literature, there are no studies on tailoring the hydrophobicity/hydrophilicity of the precursor solution which is proven in this study to be a very significant parameter that controls the HP solution crystallization. The commonly used perovskite precursor solutions are made in polar solvents such as dimethylformamide (DMF), dimethyl sulfoxide and *n*-methyl-2-pyrrolidone, and thus exhibit very hydrophilic nature. This solution hydrophilicity is expected to have a 'double-edged-sword' effect on the HP thin film crystallization. It offers the inherent merit of solution-wetting on the substrate, but at the same time leads to high nucleation density and correspondingly a high-density grain boundary network in the final thin films.[9,10] Obviously, there are opportunities to achieve large-grain thin films while maintaining the film uniformity by optimizing the hydrophobicity/hydrophilicity of the precursor solution. Note that Bi *et al.*[11] studied the effect of substrate-hydrophobicity on the wetting of the perovskite precursor solution, but this effect may have limited applications to perovskite devices with versatile architectures. In this study, we demonstrate the use of a fluorinated ionic liquid additive, methylammonium trifluoroacetate ($MA^+CF_3COO^-$, MA^+TFA^-), to tailor the intrinsic hydrophobicity of the solution and modulate grain growth of perovskite thin films. MA^+TFA^- clearly differs from other reported additives in its unique polar-hydrophobic nature owing to the $-CF_3$ group.[12] While there may be a family of possible ionic liquids with similar functionality and the ability to tailor the solution hydrophobicity, here MA^+TFA^- serves as a proof-of-concept demonstration of solution-hydrophobicity tailoring here. It is found that MA^+TFA^- also chemically functionalizes grain boundaries *via* polar–polar interactions, leading to the passivation and stabilization of perovskite grains. PSCs processed with polar-hydrophobic MA^+TFA^- show PCE exceeding 20% and significantly enhanced ambient stability.

Fig. 1 schematically shows the grain growth and grain-boundary functionalization of $MAPbI_3$ perovskite thin films that are mediated by the MA^+TFA^- additive. As seen, MA^+TFA^- contains multiple fluorocarbon groups, which endows this compound with unique polar-hydrophobicity. We have confirmed the high solubility of MA^+TFA^- in the DMF as well as the precursor solution (40% in DMF). As shown in Fig. S1 (ESI†), 75 wt% of MA^+TFA^- can be fully dissolved in DMF, which is mostly attributed to the high polarity of this compound based on the like-dissolves-like theory.[13] Meanwhile, the hydrophobicity of MA^+TFA^- tunes the wetting of the precursor solution on the substrate, resulting in

[a] *School of Chemistry and Chemical Engineering, Tianjin Polytechnic University, Tianjin 300387, P. R. China*
[b] *School of Engineering, Brown University, Providence, Rhode Island 02912, USA. E-mail: yuanyuan_zhou@brown.edu*
[c] *Qingdao Institute of Bioenergy and Bioprocess Technology, Chinese Academy of Sciences, Qingdao 266101, P. R. China*
[d] *School of Materials and Energy, University of Electronic Science and Technology of China, Chengdu 611731, P. R. China*

† Electronic supplementary information (ESI) available: Experimental details, Fig. S1–S12 and Table S1. See DOI: 10.1039/c9cc05490a

‡ These authors contributed equally.

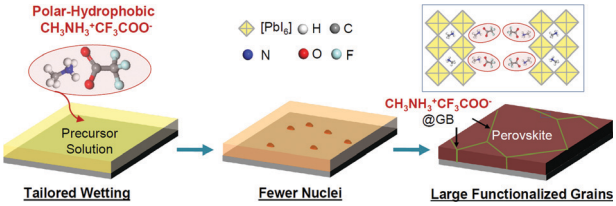

Fig. 1 Schematic representation of $MA^+CF_3COO^-$ (MA^+TFA^-) ionic liquid additive mediated crystallization and grain-boundary functionalization of $MAPbI_3$ perovskite thin films.

a high wetting angle and thus reduced heterogeneous nucleation on the substrates. The fewer nuclei grow and coalesce, resulting in $MAPbI_3$ perovskite thin films with low grain-boundary density and large grain size. While the majority of the excess MA^+TFA^- is expected to be released during thermal annealing (see thermogravimetric analysis of MA^+TFA^- in Fig. S2, ESI†), a small amount of MA^+TFA^- will be trapped at grain boundaries (see evidence later) by interacting with the methylammonium vacancies of grain surfaces considering the polarity of the MA^+TFA^- molecule. In this context, MA^+TFA^- passivates the traps at grain boundaries, and meanwhile endows the grain boundaries with hydrophobic functionality owing to the fluorocarbon groups. Furthermore, the other components (MA^+ and $-COO^-$ group) in the MA^+TFA^- additive may also be important and determine the decomposition temperatures as well as molecular-level interactions with perovskite grains.[14]

MA^+TFA^- crystals are synthesized by reacting MA^0 with trifluoroacetic acid, followed by precipitation (see ESI† for the detailed synthesis procedure). The structure of the as-synthesized MA^+TFA^- is confirmed with nuclear magnetic resonance (NMR, see Fig. S3, ESI†) and Fourier-transform infrared spectroscopy (FTIR, see Fig. S4, ESI†). In Fig. 2a and b, the wetting behaviors of the precursor solution on the substrates (compact-TiO_2-coated FTO-glasses) with and without the MA^+TFA^- addition are compared. The weight ratio of MA^+TFA^- to $MAPbI_3$ is 1 : 10. As seen, the addition of such a small amount of MA^+TFA^- increases the wetting angle from sub-5° to 30°. In Fig. S5 (ESI†), it is shown that the wetting angle is continuously increased when more MA^+TFA^- is added, implying an increase in the solution hydrophobicity. The increase in the wetting angle readily causes the growth of large grains in the thin films, as seen in the scanning electron microscope (SEM) images in Fig. 2c and d. Micrometer-size grains are observed with the addition of MA^+TFA^-. Importantly, the root-mean-square roughness of the thin film, as measured by atomic force microscopy (AFM), shows a similar small value (*ca.* 7 nm) to that for the additive-free case (Fig. 2e and f). We have also studied the effect of the amount of MA^+TFA^- on the final film morphology. We have found that perovskite grains become larger with more MA^+TFA^- addition (Fig. S6, ESI†), and a further increase in the $MA^+TFA^-/MAPbI_3$ weight ratio above 1 : 10 frequently results in incomplete film coverage. These observations are fully consistent with the overall film-growth mechanism in Fig. 1. We are also aware that MA^+TFA^- also affects the interfacial energy and chemistry of grain boundaries, which may have an effect on the grain-boundary migration kinetics and contribute to the overall grain growth. X-ray diffraction (XRD) patterns in Fig. 2g show the high phase-purity of perovskites in both thin films processed with and without a MA^+TFA^- additive. In good agreement with the grain growth, the XRD peak intensity is also significantly increased after the MA^+TFA^- addition. X-ray photoelectron spectroscopy (XPS) and energy-dispersive spectroscopy (EDS) measurements were further conducted to examine the fluorine content in the thin films. While most of the MA^+TFA^- additive has been released during the annealing process, a small amount of fluorine (F) is qualitatively observed from the XPS and EDS results (see Fig. S7 and S8, ESI†). It is deduced that the F element should be located at the grain boundaries of the thin films instead of the crystal structures, as there is no shift in XRD peak positions in Fig. 2g. We also envision that high-spatial-resolution elemental analyses of grain boundaries in perovskite thin films based on transmission electron microscopy can be performed in the future, which will be challenging but may provide deterministic understanding of element/phase distributions.[15]

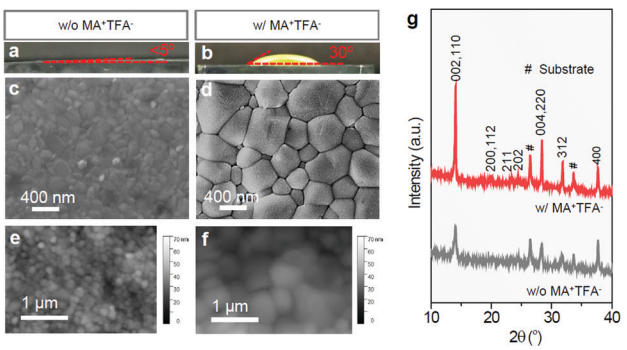

Fig. 2 Cross-sectional optical image of $MAPbI_3$ perovskite solution droplets on compact-TiO_2-coated FTO-glasses: (a) without MA^+TFA^- additive; (b) with MA^+TFA^- additive. SEM and AFM images of $MAPbI_3$ perovskite solution droplets on compact-TiO_2-coated FTO-glasses: (c and e) without MA^+TFA^- additive; (d and f) with MA^+TFA^- additive. (g) Indexed XRD patterns of $MAPbI_3$ perovskite thin films made without and with the MA^+TFA^- additive.

While the absorption characteristics of the perovskite thin film in Fig. S9 (ESI†) basically remain unchanged, the steady-state PL intensity is greatly increased under the same laser excitation conditions as shown in Fig. 3a. We further performed time-resolved PL spectroscopy to compare the PL lifetimes of the thin films with and without the MA^+TFA^- additive, and the results are shown in Fig. 3b. Both the time-resolved PL spectra can be fit using biexponential functions (see fitting parameters in Table S1, ESI†), showing average PL lifetimes (τ_{avg}) of 15.6 ns and 6.3 ns for the thin films with and without the MA^+TFA^- additive, respectively. The PL results confirm that the trap/defect density in the perovskite thin film is significantly reduced by the MA^+TFA^- additive. The trap/defect density reduction is attributed to two factors. First, the solution hydrophobicity leads to the grain growth which reduces the grain-boundary density.[16] Second, the residue MA^+TFA^- that is trapped at the grain boundary passivates the defects/traps.[17–20] We further obtained the time-resolved PL spectrum (Fig. S10, ESI†) of a perovskite thin film (made using solvent annealing) which shows a similar grain size to that of the thin film with MA^+TFA^-. The fit τ_{avg} shows a medium value of 12.2 ns, attesting

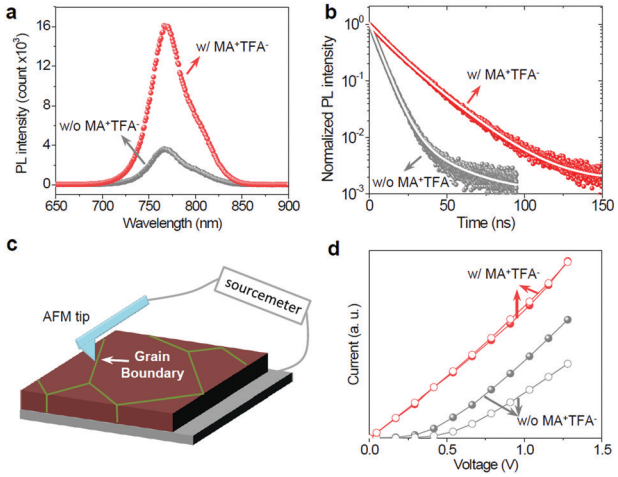

Fig. 3 (a) Steady-state and (b) time-resolved PL spectra of $MAPbI_3$ perovskite thin films made without and with the MA^+TFA^- additive. (c) Scheme for the *I–V* measurement setup at grain boundaries of the perovskite thin films. (d) *I–V* curves obtained using the setup in (c) for $MAPbI_3$ perovskite thin films made without and with the MA^+TFA^- additive. The solid and empty circles represent *I–V* results from forward (bias voltage: 0 V → 1.3 V) and reverse scans (bias voltage: 1.3 V → 0 V), respectively.

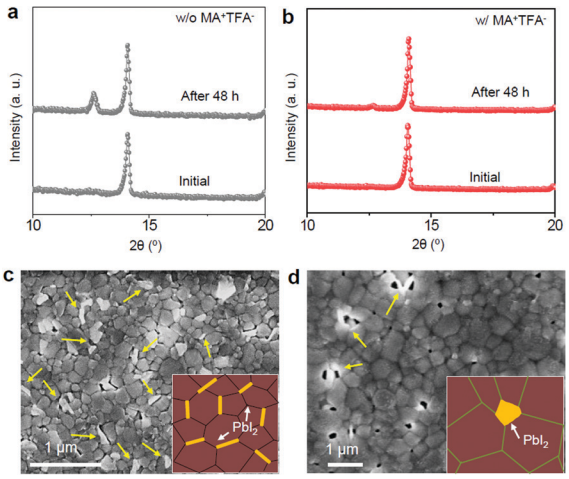

Fig. 4 XRD patterns of the $MAPbI_3$ perovskite thin film before and after 48 h exposure to the controlled humid conditions (70% RH, RT): (a) without the MA^+TFA^- additive and (b) with the MA^+TFA^- additive. Top-view SEM images of the degraded $MAPbI_3$ perovskite thin film and the corresponding schematic illustration (inset): (c) without the MA^+TFA^- additive and (d) with the MA^+TFA^- additive.

the positive effect of MA^+TFA^- grain boundary passivation in reducing non-radiative recombination. Furthermore, we compared the electronic properties of the grain boundary in the thin films without and with MA^+TFA^- using conductive AFM, respectively. The schematic illustration for the setup of this measurement is shown in Fig. 3c. Current–voltage (*I–V*) curves are measured at both forward (0 V → 1.3 V) and reverse (1.3 V → 0 V) scans. As seen in Fig. 3d, when MA^+TFA^- is present, the overall resistivity of the grain boundary is much smaller by simply comparing the slopes of the *I–V* curves. Moreover, *I–V* behavior exhibits negligible hysteresis in the presence of MA^+TFA^- at grain boundaries, which is reproducibly observed for multiple grain boundaries. This is an important sign of trap/defect passivation, because the severe hysteresis at grain boundaries in hybrid perovskite thin films is much related to the abundant defects that can trap carriers or accelerate the ion motions under electric field.[21] We are aware that the grain boundary misorientation also has some effects on the electronic behavior,[21,22] which can be much less significant than the grain boundary passivation. A rough estimation of the trap-limited voltages from the AFM based *I–V* curves suggests that the trap density at the grain boundary is reduced by a factor of two with the MA^+TFA^- additive.

The MA^+TFA^--functionalized grain boundaries benefit from the intrinsic hydrophobicity of TFA^- ions and endow the thin film with higher tolerance to the ambient moisture. Fig. 4a and b show the XRD patterns of the $MAPbI_3$ perovskite thin film before and after 48 h exposure to the controlled humid condition of 70% relative humidity (RH) at room temperature (RT). It is seen that the characteristic 001 peak evolves in the MA^+TFA^--free $MAPbI_3$ thin film, indicating that serious decomposition has occurred. In contrast, there is only slight decomposition in the MA^+TFA^- containing $MAPbI_3$ thin film. Then, the surface morphologies of both degraded $MAPbI_3$ perovskite thin films (Fig. 4c and d) are examined. Note that the perovskite grains in both thin films become coarser due to the long-time moisture exposure.[23] In the MA^+TFA^--free case, the PbI_2 crystals (plate-like) are found to be mainly located at the intergranular regions, which is consistent with the reported phenomena that the grain boundaries are where moisture ingresses and the degradation 'nucleates'.[16,24] After MA^+TFA^- functionalization, it appears that only slight decomposition of $MAPbI_3$ occurs very randomly and seemingly independent of the grain morphology. These decomposition phenomena are vividly displayed in the insets of Fig. 4c and d, and they are consistent with the fact that the grain boundaries have been functionalized with hydrophobicity and exhibit enhanced moisture resistance, and thus the overall moisture stability.

It is important to note that while the $MAPbI_3$ perovskite composition is studied for a proof-of-concept demonstration, the effect of a polar-hydrophobic ionic liquid additive on the grain growth and stabilization is generic to various perovskite compositions. In Fig. S11 (ESI†), the results for the thin films with the popularly studied formamidinium lead triiodide ($FAPbI_3$) and mixed-organic-cation $MA_{0.7}FA_{0.3}PbI_3$ perovskite compositions are shown, respectively, again confirming enhanced grain size and stability with MA^+TFA^- functionalization.

PSC devices are then fabricated to evaluate the impact of the MA^+TFA^- additive on the photovoltaic performance of $MAPbI_3$ perovskite thin films. Fig. 5a shows a cross-sectional SEM image of one typical device made with MA^+TFA^-, showing the device structure clearly. In Fig. 5b, the best-performing *J–V* curves (reverse scan) of PSCs made without and with the MA^+TFA^- additive are shown. The extracted *J–V* parameters are summarized in the inset of Fig. 5b. The overall PCE increases from 17.9% to 20.1% after the MA^+TFA^- addition, and the most obviously improved parameter is open circuit

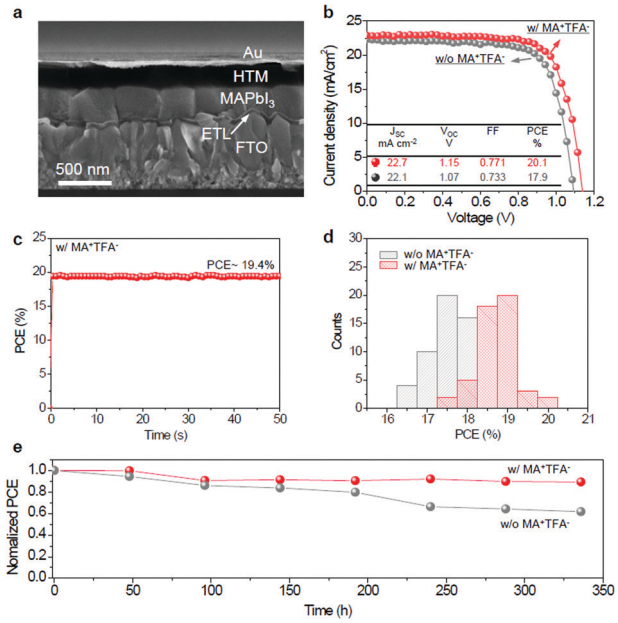

Fig. 5 (a) Cross-sectional SEM image of one typical PSC device made with MA^+TFA^-. (b) *J–V* curves of the best PSCs made without and with the MA^+TFA^- additive. The inset shows the extracted *J–V* parameters. (c) The stabilized PCE output at a maximum power point of the PSC made with the MA^+TFA^- additive. (d) PCE statistics of the typical PSCs made without and with the MA^+TFA^- additive. (e) Ambient-stability plots of the typical PSCs made without and with the MA^+TFA^- additive.

voltage (V_{OC}) that increases from 1.07 V to 1.15 V. This is consistent with the suppression in non-radiative recombination in the perovskite thin films made with MA^+TFA^- as suggested by the PL results. The typical *J–V* hysteresis curves for both devices are compared in Fig. S12 (ESI†). It is obviously seen that MA^+TFA^- reduces the hysteresis, which is consistent with the result in Fig. 3d and attests the grain boundary passivation effect. For the PSC with MA^+TFA^-, the stabilized PCE output monitored at the maximum power point (determined from the reverse *J–V* scan) is shown in Fig. 5c, delivering a stable value of about 19.4%. The PCE statistics in Fig. 5d confirm the high reproducibility of the PCE enhancement by the MA^+TFA^- addition. Fig. 5e compares the ambient stability of the typical PSCs made without and with the MA^+TFA^- additive. After 336 h of storage in the controlled ambient environment (40% RH, RT), the MA^+TFA^--functionalized PSC shows an impressively small decay of only 11%, compared to 38% for the MA^+TFA^- free case. While all the device results have proven the efficacy of the MA^+TFA^- approach, the use of the state-of-the-art perovskite compositions instead of $MAPbI_3$ in the devices may lead to higher PCE and more promising stability.

The ion-liquid-induced grain growth and stabilization opens a new possibility for tailoring halide-perovskite properties. This new chemical concept will be not limited to the application to solar cells, but a wide range of (opto)electronic devices. It can also be extended for solution synthesis of other functional materials.

We acknowledge the funding from the National Science Foundation (OIA-1538893) and Office of Naval Research (N00014-17-1-2232), as well as the support from the Advanced Ceramics and Nanomaterials Laboratory led by Prof. Nitin P. Padture.

Conflicts of interest

There are no conflicts to declare.

Notes and references

1 Y. Rong, Y. Hu, A. Mei, H. Tan, M. I. Saidaminov, S. I. Seok, M. D. McGehee, E. H. Sargent and H. Han, *Science*, 2018, **361**, eaat8235.
2 M. Lee, J. Teuscher, T. Miyasaka, T. N. Murakami and H. J. Snaith, *Science*, 2012, **338**, 643.
3 A. Kojima, K. Teshima, Y. Shirai and T. Miyasaka, *J. Am. Chem. Soc.*, 2009, **131**, 6050–6051.
4 https://www.nrel.gov/pv/cell-efficiency.html, accessed on Aug. 11, 2019.
5 J. Hamill, Jr, J. Schwartz and L. Loo, *ACS Energy Lett.*, 2018, **3**, 92.
6 Y. Zhou, M. Yang, W. Wu, A. L. Vasiliev, K. Zhu and N. P. Padture, *J. Mater. Chem. A*, 2015, **3**, 8178–8184.
7 N. K. Noel, M. Cogiu, A. J. Ramadan, S. Fearn, D. P. McMeekin, J. B. Patel, M. B. Johnston, B. Wenger and H. J. Snaith, *Joule*, 2017, **1**, 328–343.
8 D. H. Shen, X. Yu, X. Cai, M. Peng, Y. Z. Ma, X. Su, L. X. Xiao and D. C. Zou, *J. Mater. Chem. A*, 2014, **2**, 20454–20461.
9 Y. Zhou, O. S. Game, S. Pang and N. P. Padture, *J. Phys. Chem. Lett.*, 2015, **6**, 4827–4839.
10 W. A. Dunlap-Shohl, Y. Zhou, N. P. Padture and D. B. Mitzi, *Chem. Rev.*, 2019, **119**, 3193–3295.
11 C. Bi, Q. Wang, Y. Shao, Y. Yuan, Z. Xiao and J. Huang, *Nat. Commun.*, 2015, **6**, 7747.
12 (*a*) J. C. Biffinger, H.-W. Kim and S. G. DiMagno, *ChemBioChem*, 2004, **5**, 622–627; (*b*) D. Yang, X. Zhou, R. Yang, Z. Yang, W. Yu, X. Wang, C. Li, S. Liu and R. P. H. Chang, *Energy Environ. Sci.*, 2016, **9**, 3071–3078.
13 L. Pauling, *General Chemistry (Dover Books on Chemistry)*, Dover Publications, 3rd revised edn, 1988.
14 L. Chao, Y. Xia, B. Li, G. Xing, Y. Chen and W. Huang, *Chem*, 2019, **5**, 995–1006.
15 Y. Zhou, H. Sternlicht and N. P. Padture, *Joule*, 2019, **3**, 641–661.
16 F. Ji, S. Pang, L. Zhang, Y. Zong, G. Cui, N. P. Padture and Y. Zhou, *ACS Energy Lett.*, 2017, **2**, 2727–2733.
17 X. Zheng, B. Chen, J. Dai, Y. Fang, Y. Bai, Y. Lin, H. Wei, Z. Cheng and J. Huang, *Nat. Energy*, 2017, **1**, 17102.
18 T. Niu, J. Lu, R. Munir, J. Li, D. Barrit, X. Zhang, H. Hu, Z. Yang, A. Amassian, K. Zhao and A. Liu, *Adv. Mater.*, 2018, **30**, 1706576.
19 (*a*) Y. Zong, Y. Zhou, Y. Zhang, L. Zhang, M.-G. Ju, M. Chen, S. Pang, X. C. Zeng and N. P. Padture, *Chem*, 2018, **4**, 1404–1415; (*b*) Y. Zong, Z. Zhou, M. Chen, N. P. Padture and Y. Zhou, *Adv. Energy Mater.*, 2018, **8**, 1800997.
20 Q. Chen, H. Zhou, Y. Fang, A. Z. Stieg, T.-B. Song, H.-H. Wang, X. Xu, Y. Liu, S. Lu, J. You, P. Sun, J. Mckay, M. S. Goorsky and Y. Yang, *Nat. Commun.*, 2015, **6**, 7269.
21 Y. Shao, Y. Fang, T. Li, Q. Wang, Q. Dong, Y. Deng, Y. Yuan, H. Wei, M. Wang, A. Gruverman, J. Shield and J. Huang, *Energy Environ. Sci.*, 2016, **9**, 1752–1759.
22 S. Jariwala, H. Sun, G. W. P. Adhyaksa, A. Lof, E. C. Garnett and D. S. Giner, 2019, arXiv:1903.11033.
23 J. Huang, S. Tan, P. D. Lund and H. Zhou, *Energy Environ. Sci.*, 2017, **10**, 2284–2311.
24 Q. Wang, B. Chen, Y. Liu, Y. Deng, Y. Bai, Q. Dong and J. Huang, *Energy Environ. Sci.*, 2017, **10**, 516–522.

